Fibers and Polymers 2015, Vol.16, No.2, 449-462
DOI 10.1007/s12221-015-0449-3

ISSN 1229-9197 (print version)
ISSN 1875-0052 (electronic version)

Studies on Melt Spinning of Sea-island Fibers. II. Dynamics of Melt Spinning of Polypropylene/polystyrene Blend Fibers

Long Chen†, Houkang He†*, Yu Zhang*, Yanmo Chen, and Meifang Zhu

State Key Laboratory for Modification of Chemical Fibers and Polymer Materials, College of Material Science and Engineering, Donghua University, Shanghai 201620, P. R. China

(Received April 12, 2014; Revised July 16, 2014; Accepted November 3, 2014)

Abstract: A two-dimensional (2-D) model for melt spinning of iPP/aPS blend fibers is proposed based on two-phase models on density and crystallinity and log-additive rule on elongational viscosity. A computer program is developed based on a hybrid method of fourth-order Runge-Kutta method and implicit Crank-Nicolson method to solve the model equations to obtain the axial profiles of fiber diameter, velocity, gradient of velocity and crystallinity, and the 2-D profiles of temperature, elongational viscosity and elongational stress. The simulated fiber diameters are compared with the measured diameters to verify the certainness of the simulation. The simulated results show that polymer melt jets solidify at the positions of about 40 cm beneath the spinneret which is verified by on-line measurement of fiber diameter. And the radial gradient of temperature, elongational viscosity and elongational stress reaches to 10^4 to 10^5 °C/m, 10^5 to 10^6 Pa·s/m and 10^5 to 10^6 Pa/m, respectively, at the discussed take-up velocities.

Keywords: Isotactic polypropylene/atactic polystyrene, Non-isothermal melt spinning, Two-dimensional (2-D) distribution of temperature, Fourth-order Runge-Kutta method, Implicit Crank-Nicolson method

Introduction

In melt spinning of sea-island bi-component fibers, the degrees of deformation, break-up and coalescence of droplets (or islands), which decide the evolution of morphology along the spinning line, are controlled by the local conditional parameters, such as temperature, flow strain rate (or velocity gradient), rheological stress and viscosity of the dispersed droplet and matrix. Fundamental analysis of the melt spinning process is essential to understand the mechanism of fiber formation, and is helpful for the control of morphology and properties of fiber products.

In steady non-thermal melt spinning operation, the values describing the fiber formation process, such as diameter, temperature, velocity, stress, strain rate, viscosity, and so on, change according to the distance from the spinneret (or axial position). Fundamental equations (1-D model), describing the axial distributions of diameter, velocity, temperature, stress and structures of the fiber during melt spinning process, have been proposed by Ziabicki [1], Kase *et al.* [2,3] and Han *et al.* [4-6] in the 1960s, and further developed and modified next by other authors [7-9]. Recently, Kikutani *et al.* [10] and Blanco-Rodríguez *et al.* [11] studied the axial profiles of conditional parameters of sheath-core bi-component fibers. Meanwhile, the radial variation of temperature is significant for the very low thermal conductivity of spinning polymer. Andrews [12] firstly deduced a 2-D energy balance equation and predicted the radial temperature distribution, which shows that the radial temperature gradient reaches to 4000 °C/cm. Matsuo *et al.* [13] and Hutchenson *et al.* [14] also calculated and found the radial temperature gradient is huge and affects the properties of fibers. Henson *et al.* [15] calculated 2-D temperature and stress distributions for mono-component fibers by a hybrid model of 1-D mass and momentum equations and a 2-D energy balance equation. Blanco-Rodríguez *et al.* [16] simulated 2-D distribution of temperature of bi-component fibers by solving a two-dimensional model with a modified Newtonian rheology for semi-crystalline sheath-core bi-component fibers.

Unfortunately, rare attention is being paid for on the 2-D distributions of parameters of sea-island bi-component fiber spinning process. In the present report, we propose a two-dimensional (2-D) model for melt spinning of isotactic polypropylene/atactic polystyrene (iPP/aPS) sea-island blend fibers based on two-phase models on density and crystallinity and log-additive rule on elongational viscosity, to simulate 2-D distributions of temperature, elongational viscosity and stress of iPP/aPS polymer melt jets, by a hybrid method of the fourth-order Runge-Kutta method and the implicit Crank-Nicolson method. The simulated local temperature, elongational viscosity and stress at each positions of the spinning line will be used in future studies to calculate the behaviors of deformation, break-up and coalescence of the dispersed aPS droplets during the non-isothermal melt spinning.

Model Equations

Momentum and Continuity Equations

Assuming (a) steady-state spinning, (b) the cylindrical symmetry of the fields in the polymer, (c) negligible migration of dispersed domains and (d) negligible surface tension

†L. Chen and H. He contributed equally to this work.
*Corresponding author: chemfib@sina.com
*Corresponding author: yzh@dhu.edu.cn

force, equations of continuity and momentum balance for melt spinning shown in Figure 1 can be written as:

Continuity equation [17]:

$$\frac{v(x)\pi\rho(x)[d(x)]^2}{4} = W \tag{1}$$

The density of immiscible polymer blends of iPP and aPS is assumed to agree with the two-phase model [18]

$$\frac{1}{\rho} = \frac{w}{\rho_{PP}} + \frac{(1-w)}{\rho_{PS}} \tag{2}$$

The temperature-dependent density of amorphous isotactic polypropylene ($\rho_{PP,a}$) and atactic polystyrene (ρ_{PS}) read [19]

$$\rho_{PP,a}(T) = 0.8414 - 3.79\times10^{-4}T - 3.16\times10^{-7}T^2 \ \ (T \text{ in } ^{o}\text{C}) \tag{3}$$

$$\rho_{PS}(T) = 1.067 - 5.02\times10^{-4}T - 1.35\times10^{-7}T^2 \ \ (T \text{ in } ^{o}\text{C}) \tag{4}$$

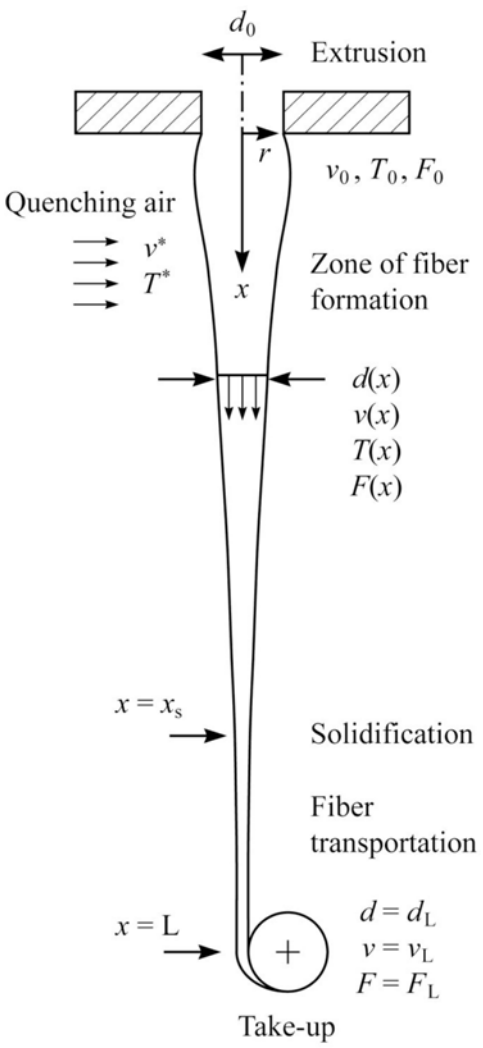

Figure 1. Schematic diagram of melt spinning.

The crystallinity-dependent density of PP in the two-phase approximation:

$$\rho_{PP}(T, X_c) = [1 - X_c(x)]\rho_{PP,a}(T) + X_{2c}(x)\rho_{PP,c} \tag{5}$$

For isotactic polypropylene, $\rho_{PP,c}$=950 kg/m^3 [20], and the temperature dependence of the crystalline component density is assumed to be negligible.

Momentum balance equation [17]:

$$\frac{dF(x)}{dx} = W\frac{dv(x)}{dx} - \frac{gW}{v(x)} + \frac{dF_{drag}(x)}{dx} \tag{6}$$

The air drag force acting on fiber with circular cross section can be written in the form [17]

$$\frac{dF_{drag}(x)}{dx} = \pi d(x)\rho^* v^2(x)c_f \tag{7}$$

The air friction coefficient used in this work is the formula with consideration of the influence of perpendicularly blowing air developed Brünig *et al*. [21]

$$c_f = \frac{a}{Re_{//}}(Re_{//}^2 + bRe_{\perp}^2)^c \text{ with}$$

$$a = 0.33, b = 4096, c = 0.2 \tag{8}$$

$$Re_{//}(x) = \frac{v(x)d(x)}{\nu^*};\ Re_{\perp}(x) = \frac{v^* d(x)}{\nu^*} \tag{9}$$

1-D Energy Balance Equation

Assuming (a) negligible radiation, (b) negligible effect of the existence of polystyrene on the crystallization behavior of polypropylene, (c) perfect amorphous state of polystyrene during all the course of melt spinning, (d) negligible viscous heat dissipation, and (e) negligible axial heat conduction, the equations of 1-D energy balance equation for the melt spinning system can be written as [17]

$$\frac{dT(x)}{dx} = -\frac{h[T(x) - T^*]\pi d(x)}{WC_p} + \frac{\Delta H_f}{C_p}\frac{dX_c(x)}{dx} \tag{10}$$

The specific heat capacity of polymer blends is determined by Appendix. According to the above assumptions (b) and (c), ΔH_f is only contributed by polypropylene and given as

$$\Delta H_f = \Delta H_{f,PP}^0 w \tag{11}$$

where $\Delta H_{f,PP}^0$ equals to 165 J/g [20,22]. The heat exchange coefficient used in this work is the formula with consideration of the influence of perpendicularly blowing air developed by Brünig *et al*. [21]

$$h = \frac{0.28\lambda^*}{d(x)}(Re_{//}^2 + 1024Re_{\perp}^2)^{0.17} \tag{12}$$

Constitutive Equation

Constitutive equation used in this work is the Maxwell model given by [17]

$$\frac{\mathrm{d}v(x)}{\mathrm{d}x}=\frac{4F(x)}{\pi d^2(x)\eta}+\frac{4v(x)}{G\pi d^2(x)}\frac{\mathrm{d}F(x)}{\mathrm{d}x} \tag{13}$$

The modulus of elasticity is dependent on temperature and crystallinity. Assuming the existence of the minor phase of polystyrene do not influence the viscoelastic behavior of major phase of polypropylene, the modulus can be expressed as [23]

$$G=G_0\exp\left[3.2\frac{X_c(x)}{X_{c,\max}}\right] \tag{14}$$

G_0 can be estimated by assuming the relaxation time τ of isotactic polypropylene as 0.035 s at 220 °C [20]. For isotactic polypropylene $X_{c,\max}$ can be assumed as 0.55 [20,24].

Apparent Elongational Viscosity

The apparent elongational viscosity of iPP/aPS blends is assumed to fulfill the log-additivity rule [25]

$$\ln\eta_{PP/PS}=w\ln\eta_{PP}+(1-w)\eta_{PS} \tag{15}$$

The apparent elongational viscosity is dependent on temperature and crystallinity. The temperature dependence is assumed in the Arrhenius form. The crystallinity dependence is assumed in Katayama's empirical equation [26]

$$\eta(T,X_c)=A\exp\left(\frac{\Delta E_\eta}{RT}\right)(1+99X_c) \tag{16}$$

The activation energy and the pre-exponential factor are assumed to be dependent on the average molecular weight and the applied elongational strain rate, and to be independent on temperature. The dependence of strain rate is determined by Appendix.

Structure Evolution Equations

The crystallization dynamics is described by the non-isothermal, quasi-static form of the Kolmogoroff-Avrami-Evans equation [27]. In this work, the simpler form with Avrami exponent $n=1$ at steady state conditions is used [17].

$$\frac{\mathrm{d}X_c(x)}{\mathrm{d}x}=\frac{K(T,f_a)}{v(x)}[1-X_c(x)] \tag{17}$$

The crystallization rate is assumed as temperature and orientation dependent and reads [20]

$$K(T,f_a)=\begin{cases}K_{\max}\exp\left[\dfrac{-4(\ln 2)(T-T_{\max})^2}{D_{1/2}^2}+C_1f_a^2\right], & T(x)<T_m^0\\ 0, & T(x)\geq T_m^0\end{cases} \tag{18}$$

For isotactic polypropylene we have $K_{\max}=0.55\ \mathrm{s}^{-1}$ [20], $T_{\max}=65$ °C [20], $D_{1/2}=60$ °C [20], $T_m^0=180$ °C [20]. C_1 is assumed appropriately to yield an estimated value of crystallinity in take-up fiber fit well with the measured one by differential scanning calorimetry (DSC).

The amorphous birefringence is assumed to satisfy the stress-optical law and reads [20]

$$\Delta n_a=C_{op}\sigma \tag{19}$$

For isotactic polypropylene, $C_{op}=9.0\times10^{-10}\ \mathrm{m^2/N}$ [20].

2-D Governing Equations

Assuming (a) constant physical properties of density, specific heat capacity, and thermal conductivity of melt, (b) negligible radial crystallinity and orientation distributions, the 2-D governing equation of energy reads [14]

$$\frac{\partial\theta}{\partial\zeta}=\frac{\partial^2\theta}{\partial\xi^2}+\frac{1}{\xi}\frac{\partial\theta}{\partial\xi} \tag{20}$$

where the dimensionless radial and axial coordinates and the dimensionless variable of temperature, respectively, are defined by

$$\xi=\frac{r}{R};\ \zeta=\frac{\pi\lambda_p x}{WC_p};\ \theta=\frac{T-T^*}{T_0-T^*} \tag{21}$$

The radial velocity distributions are assumed to be negligible as Kase [28] found that the velocity variation in radial direction was as small as $(1\sim1.03)\times10^{-6}$ in the melt spinning of polypropylene. The 2-D profile of elongational viscosity of iPP domains is calculated with equation (15) by adopting the 2-D profile of temperature. The 2-D profile of elongational stress of iPP domains is calculated by the definition equation of apparent elongational viscosity which reads

$$\eta=\frac{\sigma}{\dot{\varepsilon}} \tag{22}$$

Boundary Conditions

The following boundary conditions are assumed for the solution of 1-D model (equations (1), (6), (10), (13), (17) and (19)):

$x=0$:

$$T(0)=T_0;\ v(0)=v_0;\ d(0)=d_0;\ X_c(0)=0;\ \Delta n(0)=0 \tag{23a}$$

$x=L$:

$$v(L)=v_L \tag{23b}$$

Boundary conditions assumed for the solution of the 2-D governing equation of energy (equation (20)) as

$x=0$ (or $\zeta=0$):

$$T(r,0)=T_0;\ \theta(\xi,0)=1 \tag{24a}$$

$r = 0$ (or $\xi = 0$):

$$\frac{\partial T(0,x)}{\partial r} = 0;\ \frac{\partial \theta(0,\zeta)}{\partial \xi} = 0 \tag{24b}$$

$r = R(x)$ (or $\xi = 1$):

$$\frac{\partial T(R,x)}{\partial r} = -\frac{h}{\lambda_p}[T(R,x) - T^*];\ \frac{\partial \theta(1,\zeta)}{\partial \xi} = -\frac{hR}{\lambda_p}\theta(1,\zeta) \tag{24c}$$

Numerical Methods

Entering the boundary conditions and material constants, assuming a F_0, the differential equations (equations (6), (13) and (17)) are solved in MATLAB using the standard ODE-solver ode45.m [29], to obtain $T(x)$, $d(x)$, $v(x)$, $F(x)$, $X_c(x)$ along the spinning line position x. The routine is an implementation of an explicit Runge-Kutta method of fourth order with adaptive time step control. The assumed F_0 is corrected, until the calculated $v(L)$ satisfy the given acceptable error limit Err comparing to the actual v_L, and then the solutions are outputted. The algorithm is illustrated in Figure 2. Constants used in simulation are tabulated in Table 1.

The Crank-Nicolson method [14] is used to solve equation (20). A $Q \times M$ 2-D finite difference grid is created along the fiber axis crossing the fiber center, covering the domain of $0 \le \xi \le 1$ and $0 \le \zeta \le 1$, as shown in Figure 3. The finite difference equations presented below are then solved at each axial position to step forward incrementally down the fiber.

For the initial points of the spinning line, $n = 1$ (or $x = 0$), and equation (24a) can be rewritten as

$$\theta_{k,1} = 1 \tag{25a}$$

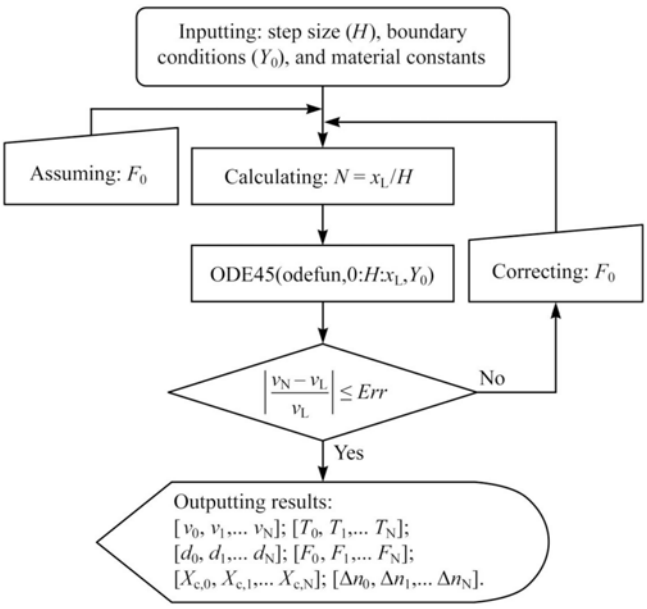

Figure 2. Algorithm for axial dynamics simulation.

For the interior points, $n > 1$ (or $x > 0$) and $2 \le k \le Q-1$ (or $0 < r < R$), and the finite difference equation is given by

$$A_k\theta_{k-1,n+1} + B_k\theta_{k,n+1} + C_k\theta_{k+1,n+1} = D_k \tag{25b}$$

where

$$A_k = k - \frac{3}{2};\ B_k = -\frac{2(k-1)(\Delta\xi)^2}{\Delta\zeta} - 2(k-1);\ C_k = k - \frac{1}{2};$$

Table 1. Constants used in numerical simulation

Parameter	Unit	Value	Ref.
Acceleration of gravity, g	m/s^2	9.8	
Heat of fusion of PP, ΔH_f	kJ/kg	165	[20,22]
Thermal conductivity of polypropylene, $\lambda_{p,PP}$	W/(m·K)	0.209	[30]
Storage modulus, G	GPa	1.40	[22]
Ziabicki rate constant at maximum crystallization rate, K_{max}	s^{-1}	0.55	[20]
Temperature of maximum crystallization rate, T_{max}	°C	65	[20]
Half-width of the Gaussian function, $D_{1/2}$	°C	60	[20]
Maximum degree of crystallinity, $X_{c,max}$	%	55	[20]
Equilibrium melting temperature of iPP, T_m^0	°C	180	[20]
Stress-optical coefficient, C_{opt}	m^2/N	9.0×10^{-10}	[20]
Maximum possible birefringence of crystalline phase, Δn_c^0		0.0291	[20]
Maximum possible birefringence of amorphous phase, Δn_a^0		0.0600	[20]
Thermal conductivity of air at 20 °C, λ^*	W/(m K)	2.591×10^{-2}	
Kinematic viscosity of air at 20 °C, ν^*	m^2/s	1.506×10^{-5}	
Density of air at 20 °C, ρ^*	kg/m^3	1.205	
Acceptable error, Err	-	1×10^{-5}	

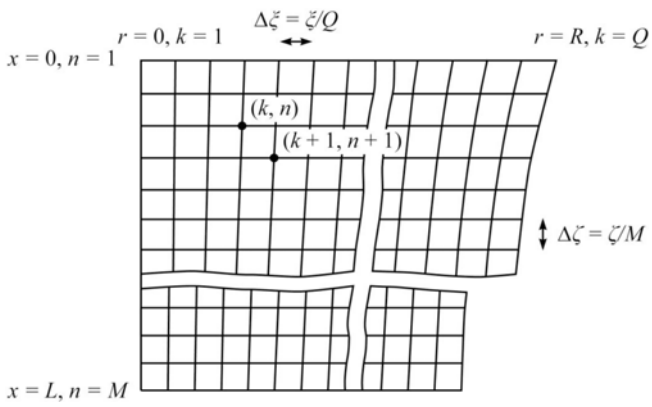

Figure 3. Schematic diagram of a 2-D finite difference grid.

$$D_k = \left[-k+\frac{3}{2}\right]\theta_{k-1,n} + \left[-\frac{2(k-1)(\Delta\xi)^2}{\Delta\zeta} + 2(k-1)\right]\theta_{k,n} + \left[-k+\frac{1}{2}\right]\theta_{k+1,n}$$

For the points at the center of fiber, $k = 1$ (or $r = 0$), and the finite difference equation is given by

$$B_1\theta_{1,n+1} + C_1\theta_{2,n+1} = D_1 \tag{25c}$$

where

$$B_1 = -2 - \frac{(\Delta\xi)^2}{\Delta\zeta};\ C_1 = 2;\ D_1 = \left[2 - \frac{(\Delta\xi)^2}{\Delta\zeta}\right]\theta_{1,n} - 2\theta_{2,n}$$

For the points on the surface of fiber, $k = Q$ (or $r = R$), the finite difference equation is given by

$$A_Q\theta_{Q-1,n+1} + B_Q\theta_{Q,n+1} = D_Q \tag{25d}$$

where

$$A_Q = 2;\ B_Q = -\frac{2(\Delta\xi)^2}{\Delta\zeta} - 2 - 2\frac{hR}{\lambda_p}\Delta\xi - \frac{hR}{\lambda_p}(\Delta\zeta)^2;$$

$$D_Q = -2\theta_{Q-1,n} + \left[-\frac{2(\Delta\xi)^2}{\Delta\zeta} + 2 + 2\frac{hR}{\lambda_p}(\Delta\xi) + \frac{hR}{\lambda_p}(\Delta\xi)^2\right]\theta_{Q,n}$$

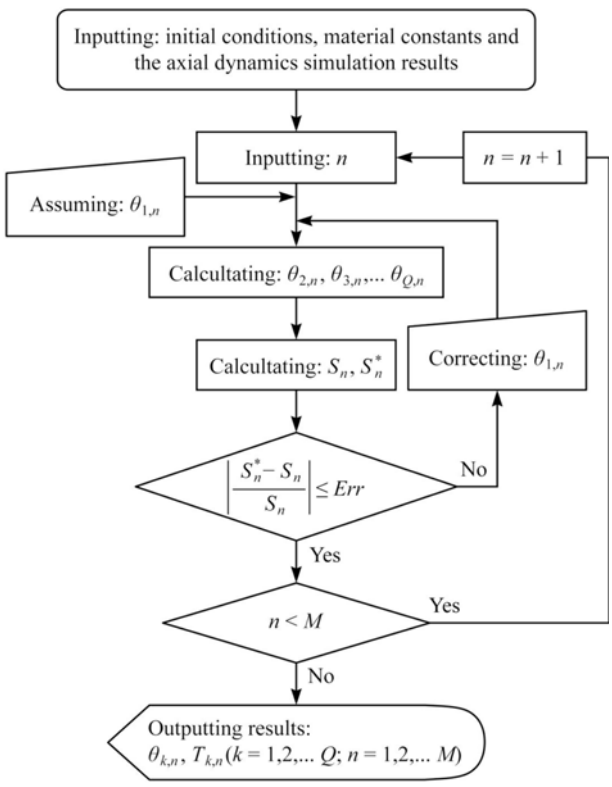

Figure 4. Algorithm for simulation of the radial temperature distribution.

Entering the material constants, the finite differential grid sizes $\Delta\xi$ and $\Delta\zeta$, the axial dynamics simulation results of fiber radius R and the heat transfer coefficient h, and the initial conditions equation (25a), assuming a dimensionless temperature of the center points $\theta_{1,2}$, the dimensionless temperatures of the remaining points $\theta_{2,2}, \theta_{3,2}\ldots\theta_{k,2}\ldots\theta_{Q,2}$ are calculated iteratively from $k = 2$ to Q by equations (25b-c). And then, the values of the left and the right of equation (24c), S_2 and S_2^*, respectively, are calculated and compared, then the assumed $\theta_{1,2}$ is corrected until the values of S_2 and S_2^* satisfy the given acceptable error limit *Err*. Then the axial grid number n ($n = 2, 3\ldots M$) is increased for repeating the above cycles till the end of the spinning line. The algorithm is illustrated in Figure 4. Constants used in simulation are tabulated in Table 1.

Material, Operating Conditions and Experimental

Material, Operating Conditions and Geometric Specifications

Raw materials iPP and aPS used in this work and their main properties are specified in the previous report [31]. Operating conditions of melt spinning and geometric specifications of spinner are also specified in the previous report [31]. The main operating conditions and geometric specifications are summarized in Table 2.

Diameters of the Polymer Melt Jets in the Spinning Line

The diameters of the polymer melt jets at different positions in the spinning line were determined using a macro photography technique. A D5000 digital SLR camera (Nikon, Japan) was used with a set of close-up filters of +4 and +10 diopters mounted in series on the primary lens. The focal

Table 2. The main processing conditions

Parameter	Unit	Specification or value
Blending ratio in weight	-	92:8 (iPP : aPS)
Single screw for melt spinning	-	D=25 mm, L/D=28, screw speed was controlled automatically to maintain the head pressure at 7±0.2 MPa
Spinneret orifice	-	D=0.30 mm, L/D=0.25
Mass throughput per orifice, W	kg/s	9.26×10^{-6}
Spinneret orifice, T_0	°C	220
Length of spinning line, x_L	cm	150
Take-up velocity, v_L	m/min	125, 250, 375, 500, 750 and 1000
Temperature of quenching air, T^*	°C	20
Velocity of quenching air, v^*	m/s	0.1

length was fixed at 55 mm. The exposure mode was set in manual, with shutter speed of 1/250 s, aperture value of f/5.6. A top flash was used, adjusting the flash angle to ensure a moderate exposure. The object was photographed clearly in a distance fixed at a very narrow scope of about 45-46 mm, and in a sharp focus with depth of field of less than 0.5 mm. This ensures the accuracy of the determination. Ten photos at each position in the spinning line were selected to count pixels of the profiles of the melt jets to calculate the diameters. The resolution of image was 2848 pixels in height, and 4288 pixels in width, and 1 pixel equals to 6.463 μm.

Crystallinity

The crystallinities of take-up fibers were determined using a 204F1 Phoenix DSC (NETZSCH, Germany). About 5 mg samples cut into powders were placed in a Al_2O_3 pan, and heated from room temperature to 250 °C in a nitrogen atmosphere at heating rate of 10 °C/min. The crystallization enthalpies during heating ΔH_{cc} and the enthalpies of fusion ΔH_m were recorded, and the crystallinities of samples X_c were calculated by

$$X_c(\%) = \frac{\Delta H_m - \Delta H_{cc}}{\Delta H_f} \times 100 \tag{26}$$

where ΔH_f is given by equation (11).

Results and Discussion

Axial Profiles of States of Polymer Melt Jets

Axial dynamics simulation step size affects the accuracy and efficiency of the program based on the algorithm shown in Figure 2. In order to set a reasonable step size, take the case of fiber taken-up at 500 m/min for instance, axial dynamics simulation is performed with serials of simulation step sizes from 5.0 to 0.15 cm. The computed gradient of velocity is shown in Figure 5. With the step size decreases, the calculation results gradually converge. Curves with step size of 1.2 cm and less almost overlap as single one. The elapsed CPU time (TOC) is used to characterize the efficiency of the program. For the uncertainness of the computer system resource allocation, 50 runs of the program with each step size are repeated, and the shortest 10 TOCs are taken for averaging. As shown in Figure 6, the average TOC is nearly in constant with the tested step sizes. To ensure a fine accuracy, a step size of 0.15 cm, which divides the spinning line into 1000 equal portions, is selected for the axial dynamics simulation in this work.

Photographs of polymer melt jets in various positions of spinning line are shown in Figure 7 (taking the case of take-up velocity of 500 m/min for instance). The measured diameters are dotted in Figure 8 comparing with the computed axial profiles of diameter. The computed axial profiles of velocity and velocity gradient of polymer melt jets are shown in

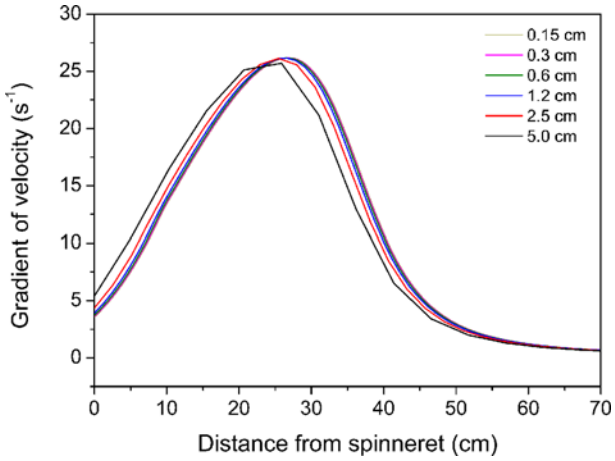

Figure 5. Simulated gradient of axial velocity with various step size (take-up velocity is 500 m/min).

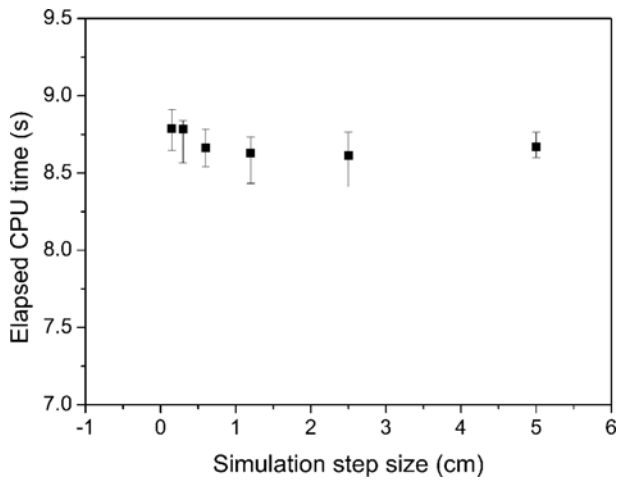

Figure 6. Elapsed CPU time versus simulation step size.

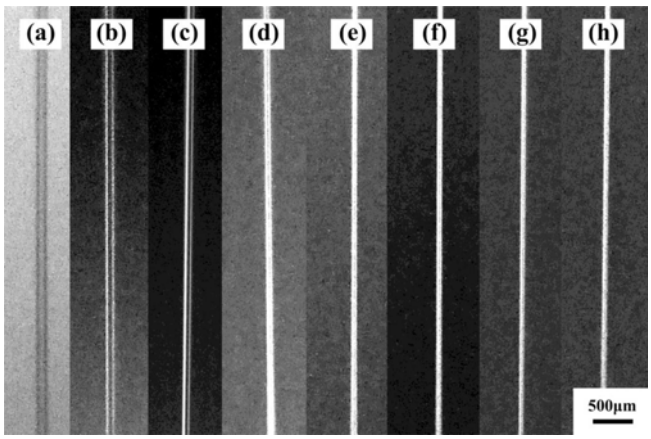

Figure 7. Photographs of running filaments token at various spinning line positions; (a) to (h) from 17.5 cm to 87.5 cm with an interval of 10 cm (take-up velocity is 500 m/min).

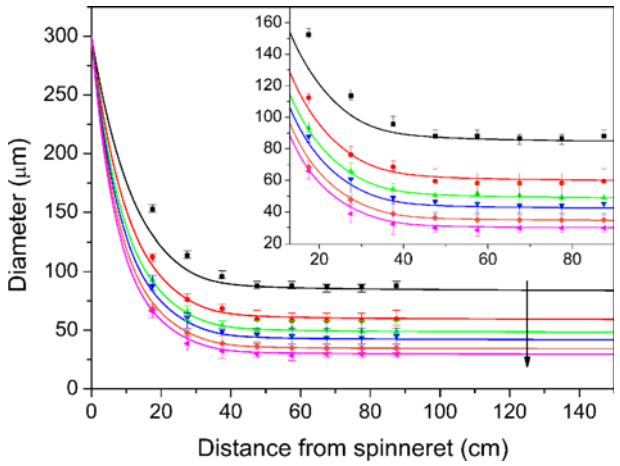

Figure 8. Filament diameters versus distance from spinneret at various take-up velocities. The arrow indicates the increase of take-up velocity from 125 to 1000 m/min.

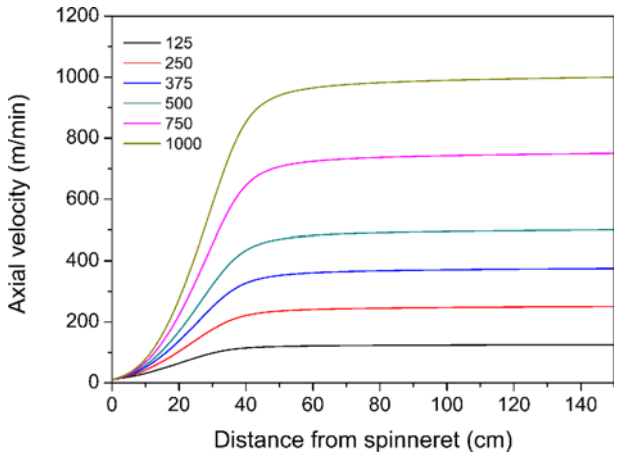

Figure 9. Filament axial velocities versus distance from spinneret.

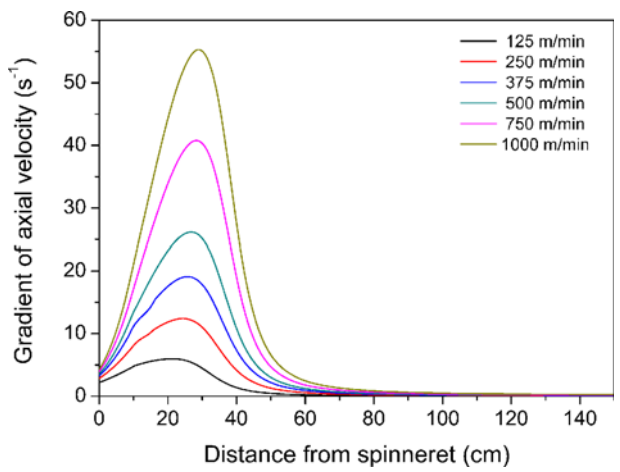

Figure 10. Gradient of axial velocities versus distance from spinneret at various take-up velocities.

Figure 9 and 10, respectively.

As shown in Figure 8 and 9, the polymer melt jets are extended thinning and accelerated from the exit of the spinneret to about 40 cm, and then become nearly constant in diameter and velocity at all of the discussed take-up velocities. The positions of around 40 cm can be referred to as "the solidification points" of the polymer melt jets. As shown in Figure 10, the maximum gradient of velocity, $(dv/dx)_{max}$, which is a function of the take-up velocity (as shown in Figure 11), arises at the positions, x_{max}, around 20 to 30 cm in the discussed take-up velocities. The empirical equations for $(dv/dx)_{max}$ and x_{max} read as:

$$(dv/dx)_{max} = 5.67\times10^{-2}v_L - 1.73 \quad (R^2 = 0.999) \tag{27}$$

$$x_{max} = 3.10\ln(v_L - 48.1) + 7.82 \quad (R^2 = 0.997) \tag{28}$$

As shown in Figure 12, crystallization starts at the positions

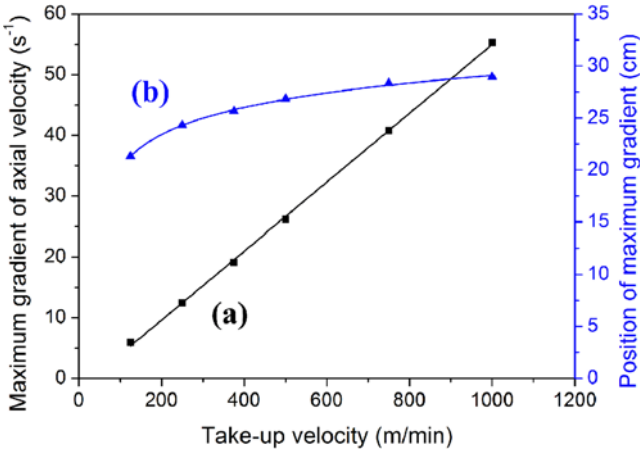

Figure 11. Maximum gradient of axial velocity (a) and position of maximum gradient (b) as functions of take-up velocity.

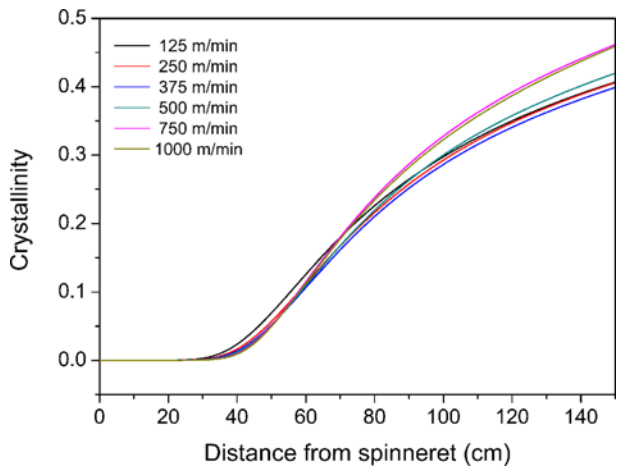

Figure 12. Crystallinity versus distance from spinneret at various take-up velocities.

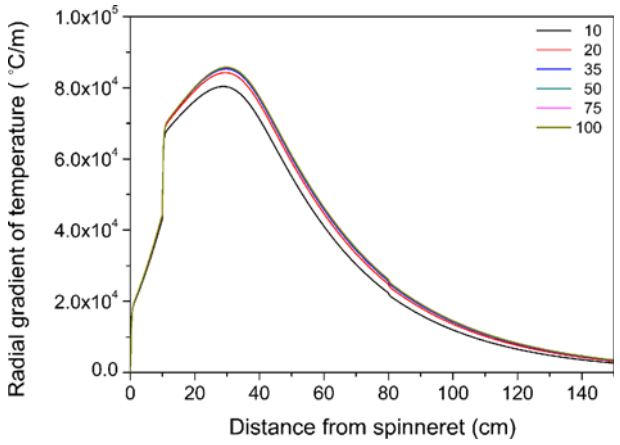

Figure 13. Simulated radial gradient of temperature with various radial meshes (take-up velocity is 500 m/min).

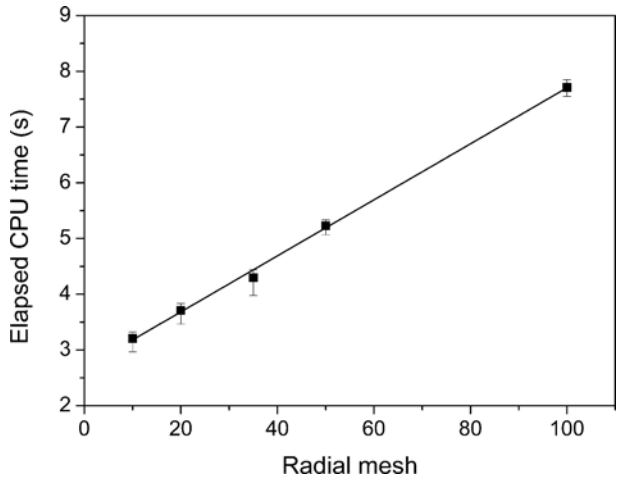

Figure 14. Elapsed CPU time versus radial meshes.

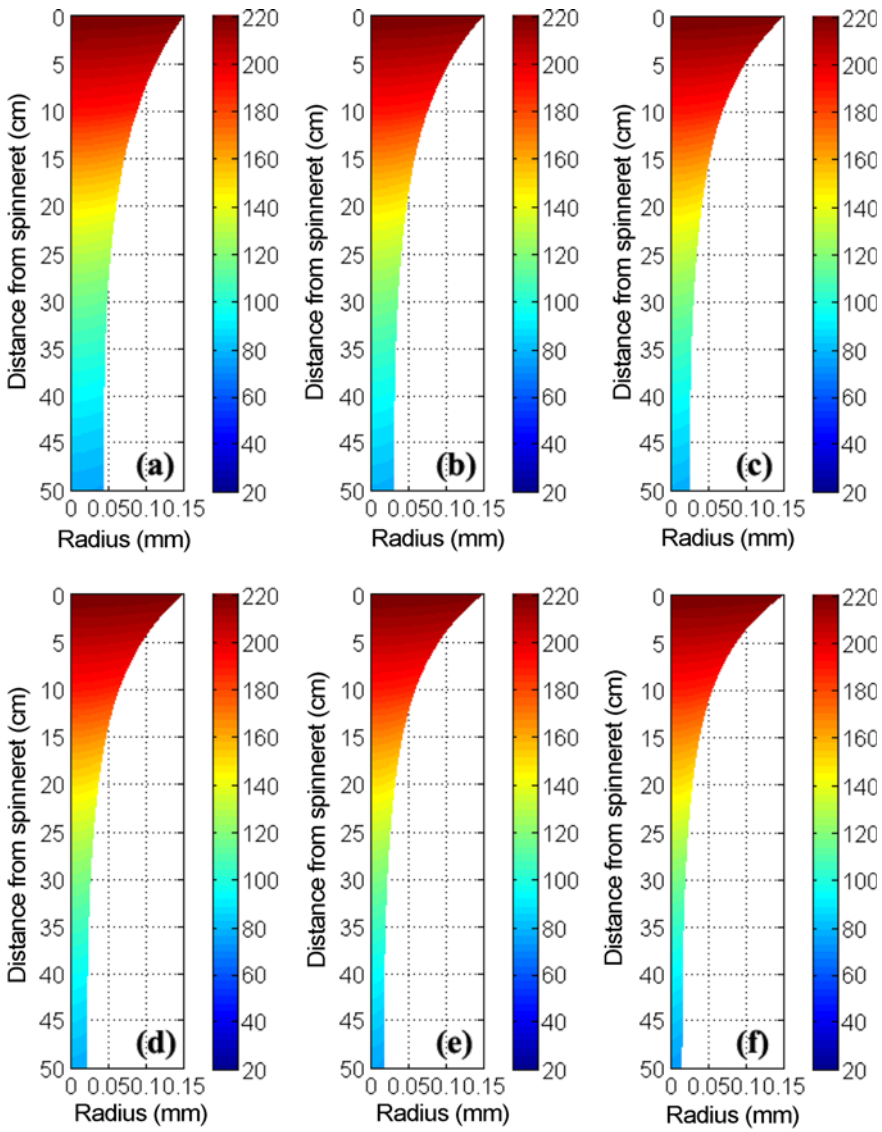

Figure 15. 2-D distributions of temperature at various take-up velocities: (a) 150, (b) 250, (c) 375, (d) 500, (e) 750, and (f) 1000 m/min.

of around 40 cm when polymer melt jets are solidified. As take-up velocity increases, flow-induced crystallization exerts its effect, and the crystallinity of take-up fiber tends to increase.

Two-Dimensional Profiles of States of Polymer Melt Jets

A 2-D finite difference grid, as shown in Figure 3, is built along the spinning line and across the center of the fiber, to solve the 2-D governing equation (equation (20)). The number of axial elements ($M-1$) is set as 1000, the same as the simulation step sizes discussed in axial dynamics simulations. The number of radial elements ($Q-1$) is set to examine the convergence and efficiency of the program based on the algorithm shown in Figure 4. Taking 500 m/min as an instance, the computed radial gradient of temperature $\partial T/\partial r$ and the TOC, with a serial of $Q-1$ of 10, 20, 35, 50, 75 and 100, are obtained and plotted in Figure 13 and 14.

As shown in Figure 13, the curves of computed radial gradient of temperature of the polymer melt jets practically overlap when $Q-1$ is not less than 35. TOC is a linear function of $Q-1$, as shown in Figure 18. For a reasonable accuracy and efficiency of the program, $Q-1$ in this work is selected as 50.

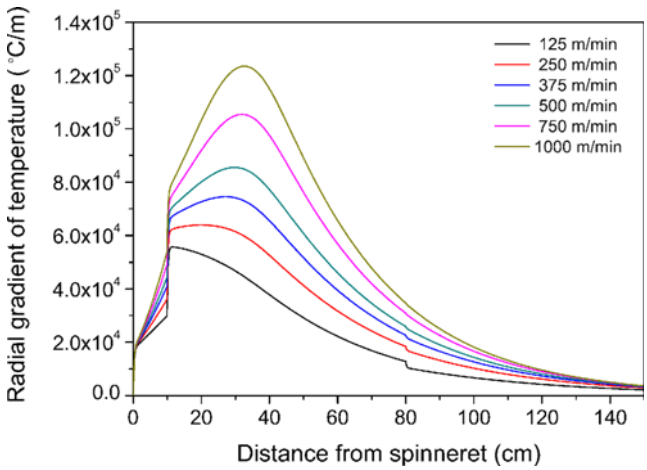

Figure 16. Radial gradient of temperature versus distance from spinneret at various take-up velocities.

The computed 2-D profiles of temperatures in polymer melt jets are shown in Figure 15. The polymer melt jets exit the spinneret at uniform temperatures. As the polymer melt jets drawn down, the polymer melt jets are cooled down, with gradients of temperatures on radial direction – transition from the central region with high temperatures to the surface region with low temperatures. The radial gradients of temperatures are shown in Figure 16. The maximum radial gradients and differences of temperatures are summarized in Table 3. The maximum radial temperature gradients vary from 5.6×10^4 to 12.4×10^4 °C/m at the positions varying from 11.4 to 32.7 cm with regard to the various take-up velocities. Moreover, the maximum radial temperature differences reach to about 4.1 to 4.7 °C at the same position of x=10.8 cm at all take-up velocities.

The 2-D profiles of elongational viscosities of the iPP domains computed from the Arrhenius equation with a consideration of the effects of crystallization (equation (16)) are shown in Figure 17. The core regions of the polymer melt jets with higher temperatures have lower viscosities, while the surface regions of the polymer melt jets with lower temperatures have higher viscosities.

As shown in Figure 18, the radial gradients of elongational viscosities of iPP domains increase rapidly from very low at the position of around 40 cm to a maximum at the position of around 90 cm and then decrease gently. The maximum radial gradients of elongational viscosities vary from about 5×10^5 to 1.5×10^6 Pa·s/m with regard to the various take-up velocities.

The elongational stresses of iPP domains are computed by the definition equation of apparent viscosity (equation (22)) and are plotted in Figure 19. Computed results show the elongational stresses of iPP domains increase rapidly from very low at the exit of spinneret (x = 0) to maximums at the position of around 40 cm, and then decrease gently. The maximum radial gradients of elongational stresses vary from about 2×10^5 to 2.2×10^6 Pa/m with regard to the various take-up velocities.

Table 3. The maximum radial gradient and difference of temperatures

v_L (m/min)	The maximum radial temperature gradient ($\partial T/\partial r$)				The maximum radial temperature difference (ΔT)			
	x (cm)	T_{core} (°C)	$T_{surface}$ (°C)	$\partial T/\partial r$ ($\times10^{-4}$ °C/m)	x (cm)	T_{core} (°C)	$T_{surface}$ (°C)	ΔT (°C)
125	11.4	184.5	179.9	5.6	10.8	187.7	183.0	4.7
250	19.8	148.4	145.4	6.4	10.8	187.0	182.6	4.5
375	27.3	125.6	123.2	7.5	10.8	186.6	182.3	4.3
500	29.7	119.3	116.9	8.6	10.8	186.3	182.0	4.2
750	32.0	112.9	110.7	10.5	10.8	185.9	181.7	4.1
1000	32.7	110.2	107.9	12.4	10.8	185.5	181.5	4.1

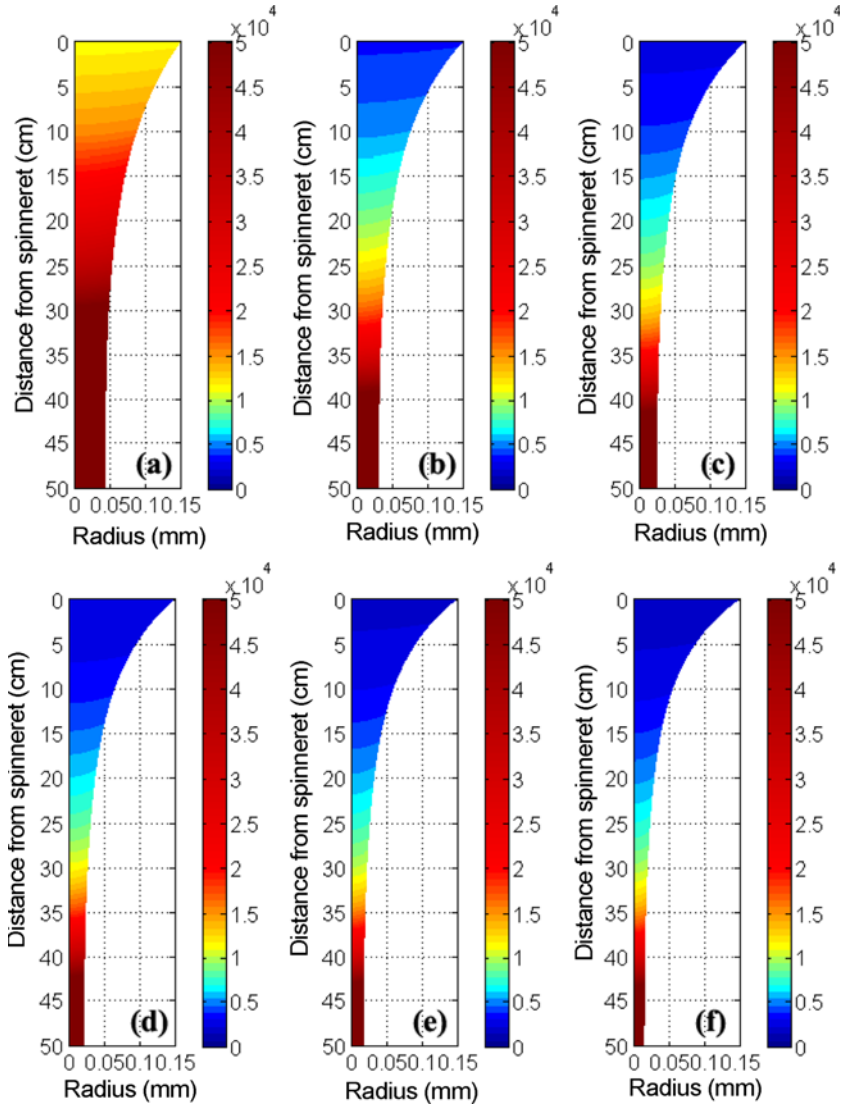

Figure 17. 2-D distributions of elongation viscosity of iPP domains at various take-up velocities: (a) 150, (b) 250, (c) 375, (d) 500, (e) 750 and (f) 1000 m/min.

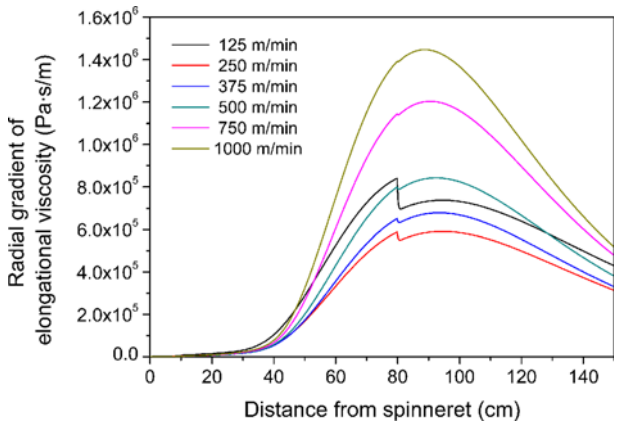

Figure 18. Radial gradient of elongational viscosity of iPP domains versus distance from spinneret at various take-up velocities.

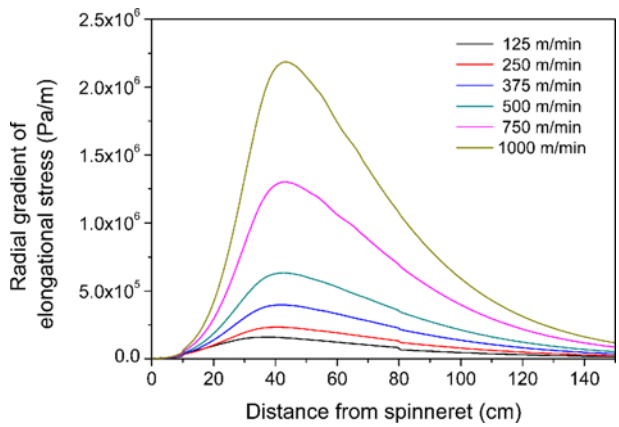

Figure 19. Radial gradient of stress of iPP domains versus distance from spinneret at various take-up velocities.

Conclusion

In this paper, we propose the basic dynamics governing equations and 2-D finite difference equations for melt spinning of iPP/aPS blends, based on two-phase models on density and crystallinity and log-additive rule on elongational viscosity. The model equations account for the effects of viscoelasticity and stress-induced crystallization in the rheological behavior of polymer blends in melt spinning. We develop a computer program based on a hybrid method of fourth-order Runge-Kutta method and implicit Crank-Nicolson method to solve the equations, and obtain the axial profiles of fiber diameter, velocity, gradient of velocity and crystallinity, and 2-D profiles of temperature, elongational viscosity and elongational stress, by imputing the measured temperature dependence of heat capacity of polymer blends and strain rate dependence of elongational rheological properties. The simulated results show that polymer melt jets solidify at the positions of about 40 cm beneath the spinneret which is verified by on-line measurement of fiber diameter. And the radial gradient of temperature, elongational viscosity and elongational stress reaches to 10^4 to 10^5 °C/m, 10^5 to 10^6 Pa·s/m and 10^5 to 10^6 Pa/m, respectively, at the discussed take-up velocities.

Acknowledgments

The authors thank the National Natural Science Foundation of China (50903013), the Fundamental Research Funds for the Central Universities (12D10610 and 13D110614) and the National Natural Science Foundation for Distinguished Young Scholar of China (50925312) for financial support.

References

1. A. Ziabicki, "Fundamentals of Fibre Formation: The Science of Fibre Spinning and Drawing", pp.159-251, Wiley, New York, 1976.
2. S. Kase and T. Matsuo, *J. Polym. Sci. Pol. Chem.*, **3**, 2541 (1965).
3. S. Kase and T. Matsuo, *J. Appl. Polym. Sci.*, **11**, 251 (1967).
4. C. D. Han and R. R. Lamonte, *J. Rheol.*, **16**, 447 (1972).
5. R. R. Lamonte and C. D. Han, *J. Appl. Polym. Sci.*, **16**, 3285 (1972).
6. C. D. Han, R. R. Lamonte, and Y. T. Shah, *J. Appl. Polym. Sci.*, **16**, 3307 (1972).
7. J. Shimizu, N. Okui, and Y. Imai, *Sen-I Gakkaishi*, **35**, 405 (1979).
8. H. H. George, *Polym. Eng. Sci.*, **22**, 292 (1982).
9. A. K. Doufas, A. J. McHugh, and C. Miller, *J. Non-Newton. Fluid Mech.*, **92**, 27 (2000).
10. J. Radhakrishnan, T. Kikutani, and N. Okui, *Text. Res. J.*, **67**, 684 (1997).
11. F. J. Blanco-Rodríguez and J. I. Ramos, *Int. J. Therm. Sci.*, **58**, 102 (2012).
12. E. H. Andrews, *Brit. J. Appl. Phys.*, **10**, 39 (1959).
13. T. Matsuo and S. Kase, *Sen-I Gakkaishi*, **24**, 512 (1968).
14. K. W. Hutchenson, D. D. Edie, and D. M. Riggs, *J. Appl. Polym. Sci.*, **29**, 3621 (1984).
15. G. M. Henson, D. Cao, S. E. Bechtel, and M. G. Forest, *J. Rheol.*, **42**, 329 (1998).
16. F. J. Blanco-Rodríguez and J. I. Ramos, *Polymer*, **52**, 5573 (2011).
17. R. Beyreuther and H. Brünig, "Dynamics of Fibre Formation and Processing: Modelling and Application in Fibre and Textile Industry", pp.47-52, Springer, 2007.
18. W. J. MacKnight, F. E. Karasz, and J. R. Fried in "Polymer Blends" (D. R. Paul and S. Newman eds.), Vol. 1, p.185, Academic Press, 1978.
19. R. Orwoll in "Physical Properties of Polymers Handbook", (J. E. Mark ed.), 2nd ed., p.93, Springer Science+Business Media, LLC, New York, 2007.
20. L. Jarecki and A. Ziabicki, *Fibres Text. East. Eur.*, **16**, 17 (2008).
21. H. Brünig, R. Beyreuther, and H. Hofman, *Int. Fiber J.*, **14**, 104 (1999).
22. D. V. Howe in "Polymer Data Handbook" (J. E. Mark ed.), p.783, Oxford University Press, 1999.
23. J. S. Lee, H. W. Jung, J. C. Hyun, and L. E. Scriven, *Aiche J.*, **51**, 2869 (2005).
24. J. S. Lee, D. M. Shin, H. W. Jung, and J. C. Hyun, *J. Non-Newton. Fluid Mech.*, **130**, 110 (2005).
25. L. A. Utracki, *Polym. Eng. Sci.*, **28**, 1401 (1988).
26. K. Katayama and M. G. Yoon in "High Speed Fiber Spinning: Science and Engineering Aspects" (A. Ziabicki and H. Kawai eds.), p.1207, John Wiley & Sons Inc., New York, 1985.
27. A. Ziabicki, *Colloid. Polym. Sci.*, **274**, 209 (1996).
28. S. Kase and M. Araki, *J. Appl. Polym. Sci.*, **27**, 4439 (1982).
29. F. Hübsch, N. Marheineke, K. Ritter, and R. Wegener, *J. Stat. Phys.*, **150**, 1115 (2013).
30. T. R. Fuller and A. L. Fricke, *J. Appl. Polym. Sci.*, **15**, 1729 (1971).
31. H. He, L. Chen, S. Sun, T. Wang, Y. Zhang, and M. Zhu, *Fiber. Polym.*, **15**, 744 (2014).
32. D. W. Wallace, C. Staudt-Bickel, and W. J. Koros, *J. Membr. Sci.*, **278**, 92 (2006).
33. F. N. Cogswell, *Polym. Eng. Sci.*, **12**, 64 (1972).

Nomenclature

A: pre-exponential factor
C_1: orientation sensitive function
c_f: air friction coefficient
C_{op}: stress-optical coefficient
C_p: specific heat capacity of polymer blends
d: diameter of polymer melt jet
$D_{1/2}$: half-width of the Gaussian function

ΔE_η: activation energy for elongational flow
F: total force
f_a: amorphous orientation factor
F_{drag}: air drag force
g: gravitational acceleration on earth
G: modulus of elasticity (equals to η/τ)
G_0: modulus of the spinning melts
h: heat exchange coefficient
ΔH_f: heat of fusion of crystalline component
$\Delta H^0_{f,PP}$: heat of fusion of perfectly crystallized isotactic polypropylene
K: crystallization rate
K_{max}: maximum crystallization rate
R: Boltzmann constant, radius of polymer melt jet
Re: non-dimensional Reynolds number
T: temperature
T^0_m : equilibrium melting temperature
T_{max}: temperature at which maximum crystallization rate achieved
v: velocity
W: mass throughput
w: mass fraction of polypropylene in the polymer blends, equals to 0.92
X_c: crystallinity
$X_{c,max}$: maximum degree of crystallinity

Greek Symbols

$\dot{\varepsilon}$: elongation strain rate
ζ: dimensionless axial coordinate
η: apparent elongational viscosity
θ: dimensionless variable of temperature
λ: thermal conductivity
ν: kinematic viscosity
ξ: dimensionless radial coordinate
ρ: density
$\rho_{PP,c}$: density of the crystalline component
σ: applied stress
τ: relaxation time

Superscripts

*: values of quenching air or simulated value

Subscripts

//: along the axial direction
⊥ : perpendicular to the axial direction
0: start point of spinning line
L: end point of spinning line
p: polymer melt jet

Appendix

Characterization of Specific Heat Capacity of iPP/aPS Melts

Characterization of specific heat capacity of melt of iPP/aPS blends was performed using a 204F1 Phoenix DSC (NETZSCH, Germany). The instrument was purged with Nitrogen (25 m*l*/min). Samples of iPP/aPS were pre-blended, dried over night under vacuum and grinded into powders of less than about 0.5 mm in diameter. Aluminum pans with the specific mass were used in the characterization. Samples for characterization were set a weight of 12.5±0.1 mg. An empty aluminum pan plus lid was used as reference. The samples were heated from room temperature to 250 °C, held at 250 °C for 15 min, cooled to 50 °C, held at 50 °C for 15 min, and then heated to 250 °C. The rate of heating and cooling was set as 10 °C/min. Heat flow rates of samples during the secondary heating were recorded and plotted. Baseline was obtained by measuring a pair of empty aluminum pans plus lids with the same procedure. Calibration was performed using a sapphire pan with the mass similar to a total mass of a sample and a set of aluminum pan and lid. The specific heat capacity was calculated by Proteus software (NETZSCH, Germany). All of the measurements were performed three times for reproducibility. The results at temperature ranging from 170 to 250 °C were selected and linear fitted as the specific heat capacity of melt of iPP/aPS blends.

The specific heat capacity of melts for equation (10) is measured as shown in Figure 20. A linear correlation between the specific heat capacity and temperature is deduced, and will be used in equation (10) to take the influence of temperature on the specific heat capacity into account.

Measurement of Elongational Rheological Properties

The elongational viscosity is critical to understand how polymers flow and deformation during melt spinning. Measurement of the elongational viscosity is difficult, but several methods have been developed to measure elongation directly or to approximate it with the use of semi-empirical models [32]. For complex spinning melts, semi-empirical

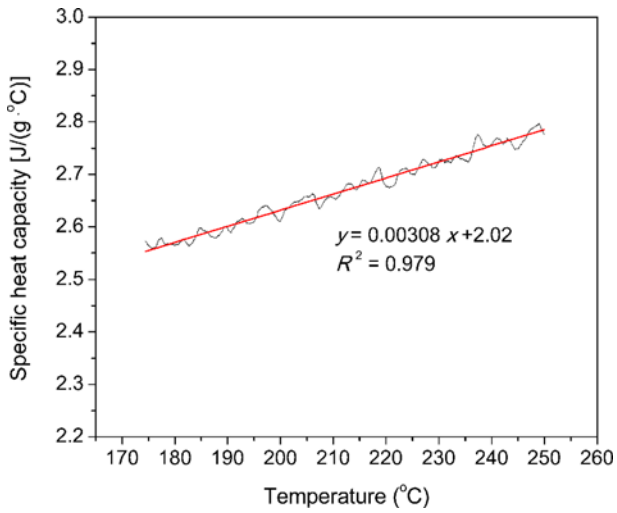

Figure 20. Specific heat capacity of iPP/aPS melts versus temperature.

methods, such as that developed by Cogswell [33], are particularly applicable. A Rosand RH2000 dual-bore capillary rheometer (Malvern Instruments, UK) is used to obtain both shear and elongational information via Cogswell's method in the same experiment, using a capillary die (D = 1 mm, L/D = 32, entry angle = 180 °) in one bore and an orifice die (D = 1 mm, L/D = 0.25, entry angle = 180 °) in the other. The equations used for the elongational strain rate ($\dot{\varepsilon}$) and the elongational viscosity (η) are given as below:

$$\dot{\varepsilon} = \frac{4\eta_s \dot{\gamma}^2}{3(n+1)\Delta P_0} \tag{29}$$

$$\eta = \frac{9(n+1)^2(\Delta P_0)^2}{32\eta_s \dot{\gamma}^2} \tag{30}$$

where η_s is the shear viscosity, n the power law exponent, ΔP_0 the orifice pressure drop, and $\dot{\gamma}$ the corrected shear rate which is given with Rabinowitsch correction as below:

$$\dot{\gamma} = \frac{3n+1}{4n}\frac{4Q}{\pi R^3} \tag{31}$$

where Q is volume flow rate, R the radius of capillary.

Elongational viscosities of PP and PS at elongation strains range from 10^1 to 10^2 at various temperatures are shown in Figure 21. The results show that the elongation viscosity of both PP and PS decreases with the increase of the elongation strain. As for melt spinning with take-up velocity under 1000 m/min, the axial velocity gradient (dv/dx) is less than 100 s^{-1}, the elongation flow curves in Figure 21 can be used to analyze the melt spinning rheology in this work.

The thermodynamic temperature dependence of elongational viscosity can be described by Arrhenius' equation at temperature much higher than the glass transaction temperature (T_g), e.g. $T > T_g + 100$ °C, and a linear fitting can be drawn between the natural logarithm of elongational viscosity and reciprocal temperature. The Arrhenius' equation is given below:

$$\eta = A\exp\left(\frac{\Delta E_\eta}{RT}\right) \tag{32}$$

where ΔE_η is the activation energy of viscous flow, A the

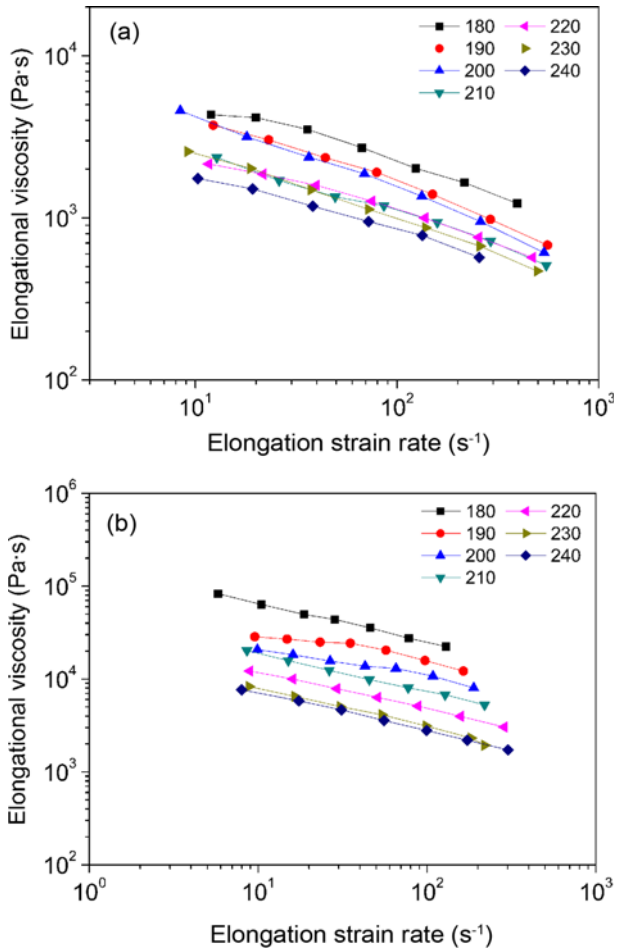

Figure 21. Apparent elongational viscosities of (a) iPP and (b) aPS as functions of applied elongation strains at various temperatures.

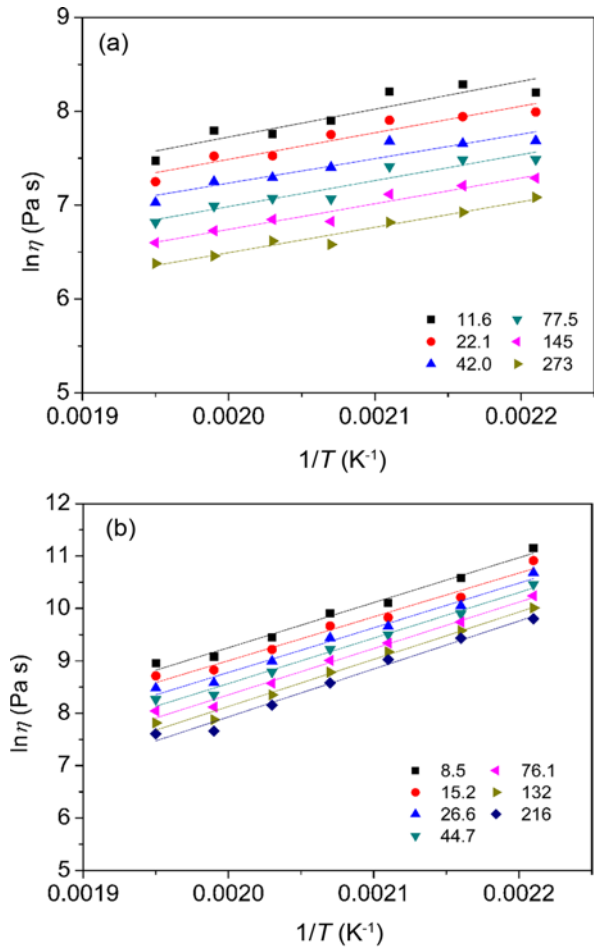

Figure 22. Arrhenius curves of (a) PP and (b) PS at various elongation strains.

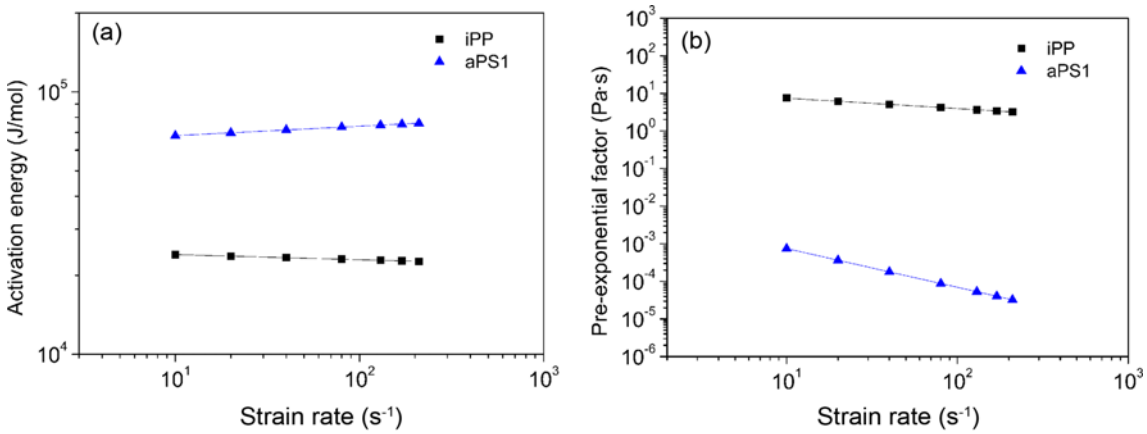

Figure 23. ΔE_η and A as functions of elongation strains; (a) ΔE_η and (b) A.

pre-exponential factor, R the gas constant. ΔE_η and A are functions of flow strains, and are independent parameters to temperature.

The elongational viscosities of PP and PS dependent on temperature are shown in Figure 22. According to equation (32), ΔE_η and A are calculated at various elongation strains and plotted in Figure 23. Linear fitting is adopted and the following equations of ΔE_η and A as functions of elongation strains are yielded.

$$\text{iPP: } \lg\Delta E_\eta = -0.0196\lg\dot{\varepsilon} + 4.3995 \tag{33a}$$

$$\text{aPS: } \lg\Delta E_\eta = 0.0359\lg\dot{\varepsilon} + 4.7975 \tag{33b}$$

$$\text{iPP: } \lg A = -0.297\lg\dot{\varepsilon} + 1.1536 \tag{34a}$$

$$\text{aPS: } \lg A = -1.0283\lg\dot{\varepsilon} - 2.0978 \tag{34b}$$